Mapping the impact of defect distributions in silicon carbide devices using the edge transient-current technique

View Online   Export Citation   CrossMark

Christian Dorfer,[a] (iD) Marianne E. Bathen, (iD) Salvatore Race, (iD) Piyush Kumar, (iD) Alexander Tsibizov, (iD) Judith Woerle, (iD) and Ulrike Grossner (iD)

AFFILIATIONS

Advanced Power Semiconductor Laboratory, ETH Zurich, Physikstrasse 3, 8092 Zurich, Switzerland

[a] Author to whom correspondence should be addressed: dorfer@aps.ee.ethz.ch

ABSTRACT

We demonstrate that the multi-photon absorption edge transient-current technique (edge-TCT) can be used to three-dimensionally map the impact of defect distributions on device characteristics *in situ* inside the bulk of silicon carbide devices. A $\sim 5\,\mu$m wide defect-rich layer induced by proton irradiation at a depth of $\sim 27\,\mu$m was investigated in 4H-SiC samples and compared to the pristine case. Edge-TCT enables mapping of the position of the implantation peak as well as to identify the space charge polarity around the implanted region. The edge-TCT results are compared to Monte Carlo simulations of the proton irradiation that were verified by luminescence measurements and TCAD-based device simulations. In result, edge-TCT is found to be capable of distinguishing different device regions due to its charge sensitivity and directly visualizing space charge regions, facilitating calibration of charge carrier distribution models in semiconductor devices.

Silicon carbide (SiC) is a popular choice for modern power electronics devices due to its excellent material properties combined with being fully CMOS compatible. However, defects in the material remain an important obstacle for reaching optimum device efficiency of SiC power semiconductors. Point defects such as the carbon vacancy and boron related impurities are inherently present in 4H-SiC epitaxial layers and have been linked to a reduction in minority carrier lifetime.[1–3] Common device processing steps such as ion implantation, thermal oxidation, and activation annealing have been shown to generate substantial defect densities[4–7] that may have an impact on device operation. The perhaps most common point defect in SiC material, the carbon vacancy (V_C), is present to concentrations of around 5×10^{12} cm^{-3} even in epitaxially grown material.[8] V_C concentrations in this range are expected to limit minority carrier lifetimes to $\sim 5\,\mu$s.[1,2] In addition to carbon vacancies, irradiated material also exhibits signals related to the silicon vacancy (V_{Si})—a known single-photon emitter and spin qubit.[9]

In this work, we demonstrate that the edge transient-current technique (edge-TCT) can be used to measure the electric field change resulting from the Si- and C-vacancy distribution within SiC with good accuracy, using proton-irradiated Schottky barrier diodes (SBDs)

as test structures. Defects in the drift layer can severely impact the charge transport through the device, and edge-TCT measurements provide explanations for the localized electric field distribution during device operation.

Figure 1 displays the schematic for the three-photon absorption edge-TCT setup that was used for the experiments (see also Refs. 10–12 for further details). A sub-percent reflection of the Ti:sapphire laser system[13] of the ETH Ultrafast Dynamics Group was used for charge excitation. The pulses reaching the focusing objective at 1 kHz repetition rate have a pulse energy of about 2 nJ, a wavelength of 800 nm, and a pulse length, taking into account dispersive pulse broadening at the optical elements, of about 113 fs. A Nikon CFI60 20× brightfield objective was used to focus the beam through the edge of the sample inside the bulk. Charge carriers are excited through three-photon absorption in an elliptical volume (cubed intensity profile of the focal point) with an estimated full width at half maximum (FWHM)-diameter of 0.7 μm and a FWHM-length of 22 μm. Under the influence of an internal or externally applied electric field, the excited carriers start to drift, which induces a current that is amplified using a CIVIDEC C6 fast charge amplifier with a gain of 5.7 mV/fC. The resulting voltage signal, which is digitized by a laser-triggered
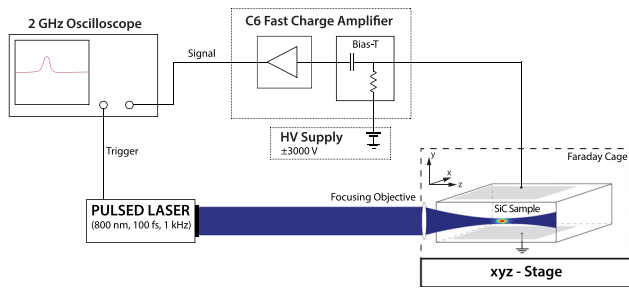
FIG. 1. Schematic of the three-photon absorption edge-TCT measurement setup. A pulsed laser is focused into the SiC device through a polished edge and excites carriers localized in the focal point. If an internal or externally applied electric field is present in the device, these carriers start drifting, which induces a current that can be amplified by a transimpedance amplifier and recorded by an oscilloscope. By scanning the sample three-dimensionally with respect to the stationary focal point, 3D maps of the charge transport properties can be extracted.

2 GHz bandwidth, 10 GS/s sampling rate Tektronix MSO5204B oscilloscope with an 8-bit pulse height resolution, is proportional to the integral of the drift current, thus the collected charge. Since the quantity of excited charge carriers does not change for a fixed penetration depth and attenuation of the laser beam, deficiencies in the amount of collected charge indicate trapping, recombination, or a change in the absolute electric field in the probed region. Three linear Newport stages driven by a Newport ESP301 motion controller allow one to move the sample relative to the stationary focal point with sub-micrometer precision at a rate of about 1 scan point per 250 ms. By scanning the sample in the xy-plane at a fixed penetration depth (z-coordinate), two-dimensional maps of the device as shown in Fig. 4 can be acquired. Performing multiple xy-scans at different z-positions enables three-dimensional scanning of the sample. The distance of the focal point relative to the device edge is measured through a knife-edge scan on a razor blade that is aligned to the edge of the sample under the microscope (accuracy $\sim$50 μm). In a first order approximation, the penetration depth of the focal point along the z-coordinate is sample movement times the refractive index of SiC. Scans at the same depth can be compared directly, while for scans at different depths, the attenuation of the laser beam when traversing the sample has to be taken into account, which requires computer simulations. The maximum penetration, and thus scanning depth, is limited by the attenuation of the laser in the sample, which, in general, depends on the wavelength of the laser and in SiC on the doping concentration of the sample. For the given samples and wavelength, scan depths in the epi-layer in excess of 1 mm were possible; however, this comes with complications such as beam loss at the device edge, thus limited the scan range coverage. To reduce noise pickup at the input of the amplifier, the sample is shielded by a copper Faraday cage. A reverse bias voltage between -200 and 0 V was applied to the Schottky contacts by a Keithley 2410 source meter.

Two samples from the same 4H-SiC wafer purchased from Ascatron were used for the experiments. The wafer has a highly n-type (8×10^{18} cm^{-3}) 4H-SiC substrate, on which a 150 μm thick epitaxial (epi)-layer was grown by chemical vapor deposition (CVD). The high-purity epi-layer is nitrogen-doped with a free carrier concentration of $\sim$2 $\times 10^{14}$ cm^{-3} as determined by capacitance–voltage measurements and has a low density of other impurities. The intrinsic carbon vacancy

(V_C) concentration in the as-grown material was 1.5×10^{11} cm^{-3} as determined by deep level transient spectroscopy (DLTS) measurements. This is more than one order of magnitude less than in conventional 10 μm thick 4H-SiC epi-layers.[8] DLTS measurements could not be performed on irradiated samples due to carrier compensation caused by a high defect density. One of the samples was exposed to a 1.8 MeV proton beam of 1×10^{12} cm^{-2} fluence at an angle of $8°$ with respect to the surface normal to avoid channeling. This energy was chosen so that the implantation and damage peaks are located far enough away from the Schottky contact while still allowing to fully deplete the region around it at moderate voltages of up to 200 V. The irradiation was performed to create defects in the material, and protons were chosen to ensure that main point defects were created instead of larger defect complexes. Note that complex formation between hydrogen and Si and C vacancies is possible in the proton implantation peak.[14] Post-irradiation annealing (PIA) was performed on the proton-implanted sample at 300 °C for 30 min in 30 ccm N$_2$ flow to alleviate some of the immediate irradiation-induced damage such as interstitial carbon and silicon (C$_i$, Si$_i$) while ensuring that the vacancy defects remained stable. Several pathways are available to the interstitials during the PIA, including recombination with vacancies and migration within the lattice. Some C$_i$ and Si$_i$ likely remain also after the annealing treatment, but their concentrations should be substantially reduced.[6] The path of the implanted hydrogen and resulting damage profiles were simulated using Monte Carlo simulations as implemented in the stopping and range of ions in matter (SRIM) code.[15] We employed a density of 3.21 g cm^{-3} for the SiC layer and displacement energies of 30 and 20 eV for Si and C, respectively (see, e.g., Ref. 16). The simulations yielded a projected range for the H ions of 26.6 μm and a straggle of around 2 μm. The peak of the Si and C vacancy distribution was predicted by SRIM to be at around the same position as the Bragg peak of the implanted protons. Assuming a dynamic annealing survival rate of 3% following irradiation and PIA at 300 °C (see, e.g., Ref. 16) yields the concentration vs depth profiles for C and Si vacancies, as depicted in Fig. 2.
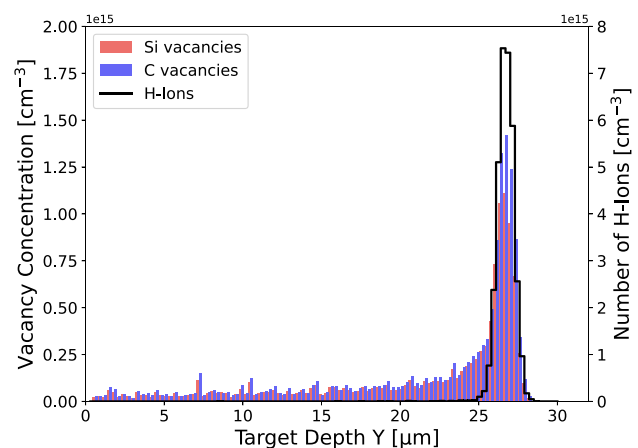

FIG. 2. The distribution of C and Si vacancies as a function of depth as determined by SRIM simulations for 1.8 MeV proton irradiation to a fluence of 1×10^{12} cm^{-2} and at $8°$ off with respect to the surface normal. The Bragg peak of implanted protons is centered at the target depth of 26.6 μm.

After PIA, one of the sides of the sample was polished, after which the native SiO_2 was removed with an HF dip. Circular Ni contacts of 150 nm thickness and a diameter varying from 300 to 700 μm were deposited onto the surface of the epi-layer to form Schottky barrier diodes (SBDs) on both samples by electron beam evaporation through a shadow mask. On the substrate side, a thin layer of Ni was deposited to form an Ohmic contact. No annealing was performed during any of the metallization steps to preserve the defect distribution.

Cross-sectional cathodoluminescence (CL) measurements were performed to verify the SRIM predictions of defect distributions using a JEOL JSM-IT300 scanning electron microscope (SEM) setup and a Delmic SPARC CL system integrated in the SEM chamber. Hyperspectral CL data were collected using an Andor Shamrock SR-193i spectrometer with a 300 l/mm grating and a charge-coupled device (CCD) Andor Newton DU940P-BU2 detector. CL spectra were measured at 80 K using probe currents in the range 0.03–0.1 nA and 10 kV acceleration voltage, which translates to approximately 200–700 nm penetration depth.

The CL false color map in Fig. 3(a) clearly shows enhanced near infrared (NIR) emission within a roughly 5 μm wide region at a distance of ~27 μm from the surface, which is in excellent agreement with the SRIM simulations (Fig. 2). In fact, the close agreement between the defect peak position estimated from the CL data and that simulated by SRIM corroborates both the validity of the SRIM model and the parameter choice made for the C and Si displacement energies. The near-infrared emission spectra in Fig. 3(b) clearly show the presence of the Si vacancy in substantial amounts within the implantation peak. Although the signal of the C vacancy has yet to be identified from luminescence spectra, we know that C and Si vacancy formation typically coincides upon irradiation,[16] which leads to comparable defect distributions (see Fig. 2). Other defects such as interstitial defects, carbon antisite-vacancy pairs, and hydrogen-related defects may also be present after the PIA, but the C and Si vacancies are assumed to be the dominant defect species. In n-type material and for 2×10^{14} cm^{-3} free carrier concentration, the Fermi level is around 0.3 eV below the conduction band edge at room temperature. This would leave the Si vacancy in the triply negative and the C vacancy in the doubly negative charge state,[16–19] essentially making the implantation peak at a depth of ~27 μm a localized and highly negatively charged region of the device.

Figure 4 shows two edge-TCT cross sections, demonstrating the amount of the collected charge, (a) in the xy-plane and (b) in the yz-plane (refer to Fig. 1 for the coordinate system), in the epi-layer below a ~700 μm diameter Schottky contact reverse-biased to 200 V in the as-grown sample. The charge collection maps clearly visualize the extent of the depleted region, in which excited carriers separate in the electric field, and nicely demonstrate the 3D imaging capabilities of the technique. The peak at y = 0 μm represents the Schottky electrode, y ≤ 0 is toward the bulk, and y ≥ 0 is toward the air. Samples are always mounted with a small tilt around the x axis [refer to Fig. 4(b)], which helps to reduce beam loss when the laser coming from the negative z-direction enters the sample close to the electrode at y = 0 μm. One of the consequences of this tilt is that the Schottky electrode is directly illuminated by the laser resulting in an excess carrier excitation at this position. We expect defects at the metal/SiC interface and reflections at the metal of the electrode to be the reason for this excess carrier excitation. Due to this effect, the position of the electrode can be determined to about 1 μm accuracy. The halo around the active
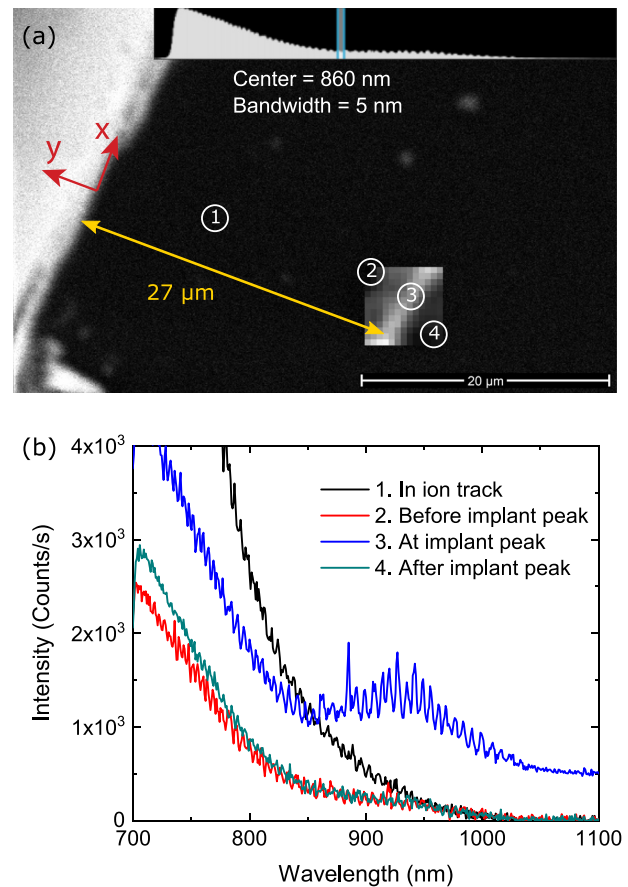

FIG. 3. (a) CL false color maps showing the intensity distribution of the near infra-red (NIR) (central wavelength of 860 nm and pixel size of 500 nm) emission. The emission range is shown in the inset. The line separating the bright and the dark regions in the top left corner is the edge of the device. (b) Representative CL spectra from the spots (1)–(4) referred to in (a) for the NIR emission. The spectra were collected at 80 K using 10 kV acceleration voltage and 0.04 nA probe current.

region that extends to areas outside the sample both in the xy- and yz-maps is due to single-photon excitation at defects in the light cone of the laser. The distribution of the electric field within the space charge region can be estimated from the charge collection map. Hence, perpendicular to the laser beam edge-TCT enables exact *in situ* monitoring to ~1 μm resolution of the active region of a device.

Charge collection profiles, which are projections of the xy-map onto the y axis over an x-range, give valuable insight into the charge collection efficiency over the depth of the sample. A charge collection profile averaged over the x-interval 283 to 293 μm below the Schottky diode on the as-grown material is shown in Fig. 5(a) for a range of reverse bias voltages. Carriers excited outside the active region of the device, e.g., at y ≤ −60 μm, do not contribute to the signal because of a lack of electric field, thus carrier drift. Significantly larger bias voltages would be needed to deplete and, thus, enable carrier drift throughout the 150 μm thick epi-layer, which was, however, limited by the quality of the fabricated Schottky diodes.
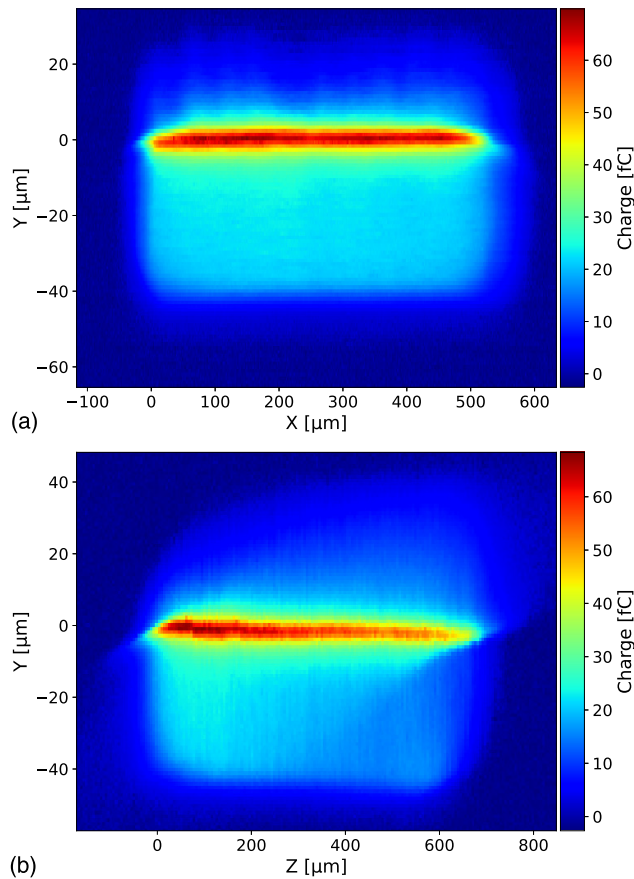
FIG. 4. Charge collection maps in the (a) xy- and (b) yz-plane below a circular 200 V reverse biased Schottky electrode on the as-grown sample. The xy-scan (a) was taken at a depth in the sample of $z = 105$ μm and the yz-scan (b) at $x = 85$ μm. In the yz-plane, the sample is intentionally tilted around the x axis by ~0.7°; this helps to reduce beam loss at the edge of the sample for scan depths at a higher z-position.
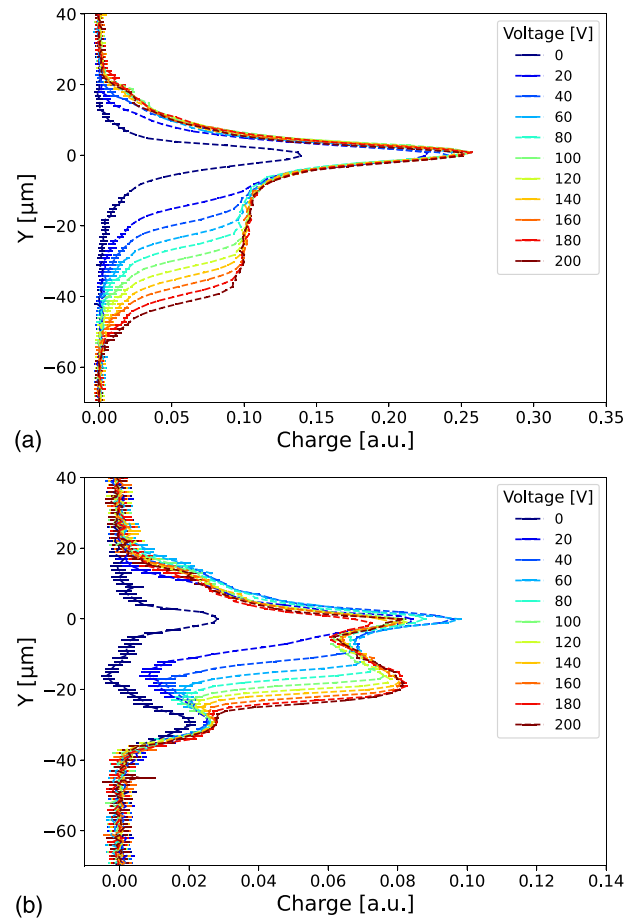

FIG. 5. Charge collection profiles as a function of depth for the (a) as-grown and (b) irradiated samples under different biasing conditions. The curves represent the average pixel signal in a 10 μm x-interval for the as-grown and for the irradiated sample. The peak at $y = 0$ μm represents the electrode, $y \leq 0$ is toward the bulk, and $y \geq 0$ is toward the air. (b) We observe an additional peak in the signal at $y = 29$ μm at all voltages in the irradiated sample attributed to the defects formed by the proton irradiation.

Figure 5(b) shows the corresponding charge collection profile for the irradiated sample. The extent of the depleted region appears to be reduced by around 10 μm, and the overall charge collection is about half of that for the as-grown sample, most likely due to effects of trapping at defects. In addition, the irradiation leads to a distinct second peak at $y = 29$ μm that is visible at all bias voltages and that coincides closely with the projected range of the proton irradiation as predicted by SRIM simulations at 26.6 μm (see Fig. 2). Comparing the post-irradiation charge collection behavior to that in the as-grown diode without applied bias as shown in Fig. 6(a), the first peak in both samples is caused by the excitation of carriers at the Schottky diode that drifts in the built-in potential of the diode. The second peak that is only present in the irradiated sample at $y = 29$ μm is due to the electric field caused by the high concentration of electrically active defects in this region.

Figures 6(a) and 6(b) reveal that, in the region from approximately $y = -10$ to $y = -20$ μm, the signal becomes negative due to a reversed electric field in the bulk of the device. The direction of the current induced by this drift is directly measurable and depends on the excitation position as shown in Fig. 6(b). Carriers excited near the Schottky contact ($y = 0$ to -5μm) induce a positive current, which indicates that electrons excited in this region drift toward the bulk and holes toward the Schottky contact. Between $y = -10$ μm and up to $y = -20$ μm, the induced current is negative, indicating that the current drift is opposite (electrons drift toward the Schottky contact and holes toward the bulk). The current direction switches again for the region $y \leq -20$ μm due to the influence of the defective region.

Simulations to compare the charge distribution and electric field in the as-grown and irradiated devices and verify that the defective region is responsible for the inverted current direction were conducted in Sentaurus TCAD based on a simplified 1D structure of the Schottky diodes. The defect distributions of the Si and C vacancies in Fig. 2 were incorporated into TCAD by fitting them with two Gaussian distributions and a constant offset for the peak and tail of the irradiation,
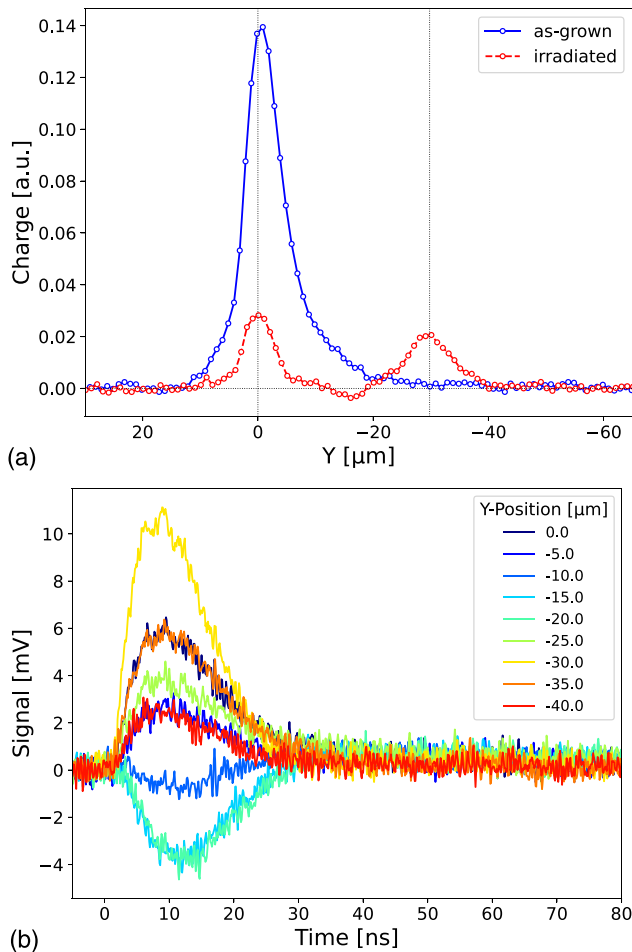
(a)

(b)

FIG. 6. (a) Charge collection profiles as a function of depth for the as-grown (blue curve) and irradiated (red curve) samples measured without any applied external voltage. The vertical lines depict the electrode at $y = 0$ μm and the peak charge collection around the implantation peak at $y = 29$ μm. (b) The polarity of the signals changes as a function of y-coordinate in the irradiated sample. In the region from approximately $y = -20$ μm to $y = -10$ μm, the signal becomes negative in the irradiated sample due to a reversed electric field in the bulk of the device.

respectively. The traps have been modeled with energy levels that were determined by DLTS measurements and theoretical calculations. The V_C exhibits a deep level labeled $EH_{6/7}$ and assigned to the $(2+/+/0)$ donor transition at 1.5–1.6 eV below the conduction band edge (E_C). The V_{Si} introduces a $(0/-)$ acceptor level in the bandgap at 1.2 eV above the valence band edge (E_V) that was theoretically predicted, and two acceptor levels at $E_C - 0.7$ and $E_C - 0.4$ eV that were experimentally assigned to the $(-/2-)$ and $(2-/3-)$ charge-state transitions, respectively.[16–20] See Fig. 7 for a schematic of the approximate positions of the V_C and V_{Si} trap energy levels in the 4H-SiC bandgap. The three distinct energy levels of the Si vacancy have been modeled as acceptor traps herein, i.e., the trap is uncharged when unoccupied and has a negative charge when occupied by an electron. The C vacancy was modeled with one acceptor and one donor trap.[18] The donor trap is uncharged when unoccupied and has a positive charge when
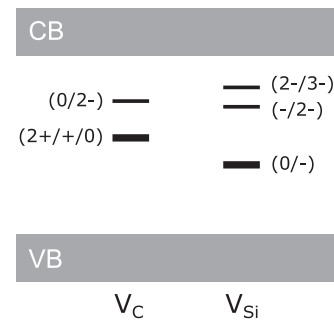

FIG. 7. Schematic of trap levels introduced in the 4H-SiC bandgap by the C and Si vacancy (V_C and V_{Si}, respectively). VB = valence band and CB = conduction band.

occupied by a hole. Note that there is a possibility that the C and Si vacancies in the implantation peak are passivated by hydrogen.[14] However, this will not change the conclusions in this paper as both the V_C–H and V_{Si}–H complexes were shown to exhibit acceptor type traps in similar regions of the bandgap as the isolated vacancies.[14,21] The concentration of trapped carriers in the irradiated sample is shown in Fig. 8(a). In the considered n-type Schottky diode, electrons are the dominant type of trapped charge. The concentration of traps is enough to capture all the free electrons, which leads to a concentration of trapped electrons at the implantation peak that is much higher than the background doping concentration ($N_D \sim 2 \times 10^{14}$ cm^{-3}).
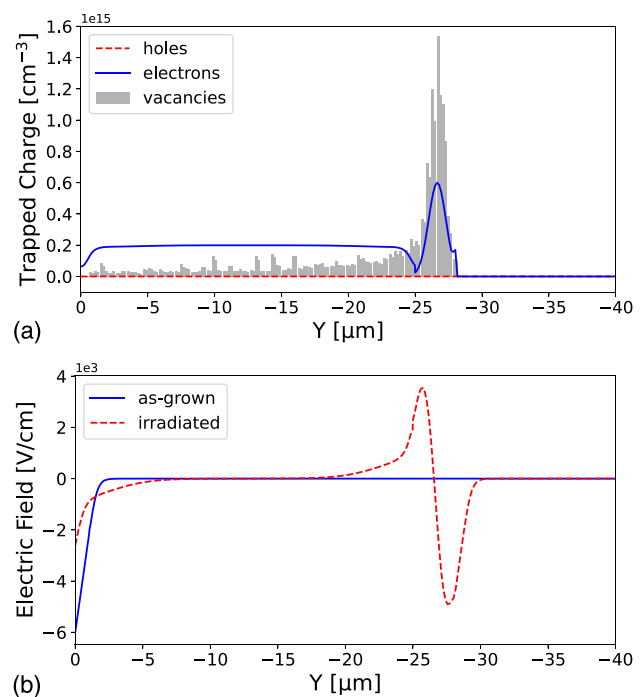

(a)

(b)

FIG. 8. (a) Trapped charge (electrons and holes) without an externally applied bias voltage for the irradiated sample. The high concentration of electrons around $y = -26.6$ μm is due to the distribution of Si and C vacancies plotted in gray (same distribution as in Fig. 2, included for clarity). (b) Electric field without an externally applied bias, note the reduced Schottky barrier in the irradiated sample.

Due to this space charge density variation, a depletion region forms around the implantation peak in the irradiated sample. The electric field switches polarity at the center of the implantation peak and is non-zero otherwise, as shown in Fig. 8(b). The charge collection profile measured by edge-TCT shown in Fig. 6(a) indicates the presence of this electric field. Even without an externally applied electric field, the electric field caused by the negative trapped charge around the implantation peak is strong enough for carriers excited in this region to induce a measurable current. In a direct comparison between the peak of the defect distribution, the trapped charge and electric field, which are all around $y = 26.6 \, \mu m$, and the peak of the charge collection observed in the edge-TCT measurement at $y = 29 \, \mu m$, a disagreement of $2.4 \, \mu m$ is observed. We expect that this deviation is due to neglecting the contribution of interstitial and other defects caused by the proton irradiation that persist even after PIA in the TCAD simulations. Interstitials are known to be mobile in SiC above room temperature[6] and may be migrating beyond the H implantation peak during the irradiation and PIA processes.

In this paper, we have shown that a highly defective region formed by proton implantation can be detected with edge-TCT at micrometer accuracy, and that it is possible to identify the direction of the electric field, thus the space charge polarity inside the device. The sensitivity in identifying implanted regions is similar to that of CL, but the measurement principle is purely electrical. Thus, edge-TCT is only sensitive to electrically active defects. Edge-TCT has a great potential for being used to map termination regions, the epi-layer, and 2D structures such as trench-pillar structures or as shown to map the defect distribution in the device as a result of different device processing steps.

AUTHOR DECLARATIONS
Conflict of Interest

The authors have no conflicts to disclose.

Author Contributions

Christian Dorfer: Conceptualization (equal); Data curation (equal); Formal analysis (equal); Investigation (equal); Methodology (equal); Project administration (equal); Resources (equal); Visualization (equal); Writing – original draft (equal); Writing – review & editing (equal). **Marianne Etzelmüller Bathen:** Conceptualization (lead); Data curation (equal); Formal analysis (equal); Funding acquisition (equal); Investigation (equal); Project administration (equal); Resources (equal); Visualization (equal); Writing – original draft (equal); Writing – review & editing (equal). **Salvatore Race:** Data curation (equal); Validation (equal). **Piyush Kumar:** Resources (equal). **Alexander Tsibizov:** Data curation (equal); Validation (equal). **Judith Woerle:** Resources (equal). **Ulrike Grossner:** Funding acquisition (lead); Project administration (equal); Resources (equal); Supervision (lead).

DATA AVAILABILITY

The data that support the findings of this study are available from the corresponding author upon reasonable request.

REFERENCES

[1] P. B. Klein, B. V. Shanabrook, S. W. Huh, A. Y. Polyakov, M. Skowronski, J. J. Sumakeris, and M. J. O'Loughlin, "Lifetime-limiting defects in n-4H-SiC epilayers," Appl. Phys. Lett. **88**, 052110 (2006).

[2] K. Danno, D. Nakamura, and T. Kimoto, "Investigation of carrier lifetime in 4H-SiC epilayers and lifetime control by electron irradiation," Appl. Phys. Lett. **90**, 202109 (2007).

[3] L. Storasta, P. Bergman, E. Janzén, and C. Hallin, "Electrical activity of residual boron in silicon carbide," in *Silicon Carbide and Related Materials 2001*, Materials Science Forum, Vol. 389 (Trans Tech Publications Ltd, 2002), pp. 549–552.

[4] J. W. Steeds, W. Sullivan, A. Wotherspoon, and J. M. Hayes, "Long-range migration of intrinsic defects during irradiation or implantation," J. Phys.: Condens. Matter **21**, 364219 (2009).

[5] T. Okuda, G. Alfieri, T. Kimoto, and J. Suda, "Oxidation-induced majority and minority carrier traps in n- and p-type 4H-SiC," Appl. Phys. Express **8**, 111301 (2015).

[6] R. M. Karsthof, M. E. Bathen, A. Galeckas, and L. Vines, "Conversion pathways of primary defects by annealing in proton-irradiated n-type 4H-SiC," Phys. Rev. B **102**, 184111 (2020).

[7] R. Karsthof, M. E. Bathen, A. Kuznetsov, and L. Vines, "Formation of carbon interstitial-related defect levels by thermal injection of carbon into n-type 4H-SiC," J. Appl. Phys. **131**, 035702 (2022).

[8] B. Zippelius, J. Suda, and T. Kimoto, "High temperature annealing of n-type 4H-SiC: Impact on intrinsic defects and carrier lifetime," J. Appl. Phys. **111**, 033515 (2012).

[9] M. Widmann, S.-Y. Lee, T. Rendler, N. T. Son, H. Fedder, S. Paik, L.-P. Yang, N. Zhao, S. Yang, I. Booker, A. Denisenko, M. Jamali, S. A. Momenzadeh, I. Gerhardt, T. Ohshima, A. Gali, E. Janzén, and J. Wrachtrup, "Coherent control of single spins in silicon carbide at room temperature," Nat. Mater. **14**, 164–168 (2015).

[10] G. Kramberger, V. Cindro, I. Mandić, M. Mikuž, M. Milovanović, M. Zavrtanik, and K. Žagar, "Investigation of irradiated silicon detectors by edge-TCT," IEEE Trans. Nucl. Sci. **57**, 2294–2302 (2010).

[11] C. Dorfer, D. Hits, L. Kasmi, G. Kramberger, M. Lucchini, M. Mikuž, and R. Wallny, "Three-dimensional charge transport mapping by two-photon absorption edge transient-current technique in synthetic single-crystalline diamond," Appl. Phys. Lett. **114**, 203504 (2019).

[12] M. E. Bathen, C. T.-K. Lew, J. Woerle, C. Dorfer, U. Grossner, S. Castelletto, and B. C. Johnson, "Characterization methods for defects and devices in silicon carbide," J. Appl. Phys. **131**, 140903 (2022).

[13] R. Locher, M. Lucchini, J. Herrmann, M. Sabbar, M. Weger, A. Ludwig, L. Castiglioni, M. Greif, M. Hengsberger, L. Gallmann, and U. Keller, "Versatile attosecond beamline in a two-foci configuration for simultaneous time-resolved measurements," Rev. Sci. Instrum. **85**, 013113 (2014).

[14] M. E. Bathen, A. Galeckas, J. Coutinho, and L. Vines, "Influence of hydrogen implantation on emission from the silicon vacancy in 4H-SiC," J. Appl. Phys. **127**, 085701 (2020).

[15] J. F. Ziegler, M. Ziegler, and J. Biersack, "SRIM – The stopping and range of ions in matter (2010)," Nucl. Instrum. Methods Phys. Res. Sect. B: Beam Interact. Mater. Atoms **268**, 1818–1823 (2010).

[16] M. E. Bathen, A. Galeckas, J. Müting, H. M. Ayedh, U. Grossner, J. Coutinho, Y. K. Frodason, and L. Vines, "Electrical charge state identification and control for the silicon vacancy in 4H-SiC," npj Quantum Inf. **5**, 111 (2019).

[17] T. Hornos, A. Gali, and B. G. Svensson, "Large-scale electronic structure calculations of vacancies in 4H-SiC using the Heyd-Scuseria-Ernzerhof screened hybrid density functional," Mater. Sci. Forum **679–680**, 261–264 (2011).

[18]N. T. Son, X. T. Trinh, L. S. Løvlie, B. G. Svensson, K. Kawahara, J. Suda, T. Kimoto, T. Umeda, J. Isoya, T. Makino, T. Ohshima, and E. Janzén, "Negative-U system of carbon vacancy in 4H-SiC," Phys. Rev. Lett. **109**, 187603 (2012).

[19]J. Coutinho, V. J. B. Torres, K. Demmouche, and S. Öberg, "Theory of the carbon vacancy in 4H-SiC: Crystal field and pseudo-Jahn-Teller effects," Phys. Rev. B **96**, 174105 (2017).

[20]M. L. David, G. Alfieri, E. M. Monakhov, A. Hallén, C. Blanchard, B. G. Svensson, and J. F. Barbot, "Electrically active defects in irradiated 4H-SiC," J. Appl. Phys. **95**, 4728–4733 (2004).

[21]J. Woerle, M. E. Bathen, T. Prokscha, A. Galeckas, H. M. Ayedh, L. Vines, and U. Grossner, "Muon interaction with negative-u and high-spin-state defects: Differentiating between C and Si vacancies in 4H-SiC," Phys. Rev. Appl. **14**, 054053 (2020).